Journal of Instrumentation

PAPER • OPEN ACCESS

# SIDDHARTA-2 apparatus for kaonic atoms research on the DAΦNE collider

To cite this article: F. Sirghi *et al* 2024 *JINST* **19** P11006

View the article online for updates and enhancements.

You may also like

- A new kaonic helium measurement in gas by SIDDHARTINO at the DANE collider
D Sirghi, F Sirghi, F Sgaramella et al.
- The SIDDHARTA-2 calibration method for high precision kaonic atoms x-ray spectroscopy measurements
F Sgaramella, M Miliucci, M Bazzi et al.
- Silicon drift detectors system for high-precision light kaonic atoms spectroscopy
M Miliucci, A Scordo, D Sirghi et al.


This content was downloaded from IP address 5.91.91.130 on 25/11/2024 at 08:28

Published by IOP Publishing for Sissa Medialab

Received: *June 17, 2024*
Revised: *August 15, 2024*
Accepted: *September 29, 2024*
Published: *November 13, 2024*

# SIDDHARTA-2 apparatus for kaonic atoms research on the DAΦNE collider

**F. Sirghi**,[a,b,*] **M. Iliescu**,[a] **L. Abbene**,[l] **C. Amsler**,[e] **M. Bazzi**,[a] **G Borghi**,[d] **D. Bosnar**,[c] **M. Bragadireanu**,[b] **A. Buttacavoli**,[l] **M. Carminati**,[d] **M. Cargnelli**,[e] **A. Clozza**,[a] **G. Deda**,[d] **L. De Paolis**,[a] **R. Del Grande**,[a,f] **K. Dulski**,[a] **L. Fabbietti**,[f] **C. Fiorini**,[d] **I. Friščić**,[c] **C. Guaraldo**,[a] **M. Iwasaki**,[i] **A. Khreptak**,[a,g] **S. Manti**,[a] **J. Marton**,[e] **P. Moskal**,[g,h] **F. Napolitano**,[a] **S. Niedźwiecki**,[g,h] **H. Ohnishi**,[k] **K. Piscicchia**,[a,j] **F. Principato**,[l] **A. Scordo**,[a] **F. Sgaramella**,[a] **D. Sirghi**,[a,b,j] **M. Skurzok**,[g,h] **M. Silarski**,[g,h] **A. Spallone**,[a] **K. Toho**,[k] **L. Toscano**,[d] **M. Tüchler**,[e] **O. Vazquez Doce**,[a] **J. Zmeskal**[e] **and C. Curceanu**[a]

[a] *Laboratori Nazionali di Frascati dell'INFN, Via E. Fermi 54, Frascati, Italy*
[b] *Horia Hulubei National Institute of Physics and Nuclear Engineering (IFIN-HH), Reactorului 30, Magurele, Romania*
[c] *Department of Physics, Faculty of Science, University of Zagreb, Bijenicka cesta 32, Zagreb, Croatia*
[d] *Politecnico di Milano, Dipartimento di Elettronica, Informazione e Bioingegneria and INFN Sezione di Milano, Via Giuseppe Ponzio 34, Milano, Italy*
[e] *Stefan-Meyer-Institut für Subatomare Physik, Dominikanerbastei 16, Vienna, Austria*
[f] *Excellence Cluster Universe, Technische Universiat Munchen Garching, Boltzmann str.2, Garching, Germany*
[g] *Faculty of Physics, Astronomy, and Applied Computer Science, Jagiellonian University, Łojasiewicza 11, Krakow, Poland*
[h] *Centre for Theranostics, Jagiellonian University, Kopernika 40, Krakow, Poland*
[i] *RIKEN, 2-1 Hirosawa, Wako, Saitama, Tokyo, Japan*
[j] *Centro Ricerche Enrico Fermi – Museo Storico della Fisica e Centro Studi e Ricerche "Enrico Fermi", Via Panisperna 89A, Roma, Italy*
[k] *Research Center for Accelerator and Radioisotope Science(RARIS), Tohoku University, 1-2-2 Mikamine, Sendai, Japan*
[l] *Dipartimento di Fisica e Chimica - Emilio Segrè, Università di Palermo, Viale Delle Scienze, Edificio 18, Palermo, Italy*

*E-mail:* fsirghi@lnf.infn.it

[*] Corresponding author.

© 2024 The Author(s). Published by IOP Publishing Ltd on behalf of Sissa Medialab. Original content from this work may be used under the terms of the Creative Commons Attribution 4.0 licence. Any further distribution of this work must maintain attribution to the author(s) and the title of the work, journal citation and DOI.

https://doi.org/10.1088/1748-0221/19/11/P11006

2024 JINST 19 P11006

Abstract: SIDDHARTA-2 is a state-of-the-art experiment designed to perform measurements of kaonic atoms, which are exotic atoms composed of a negatively charged kaon orbiting nucleus. These atoms constitute an exceptional probe for investigating the strong interaction in the non-perturbative regime involving strangeness. The experiment is installed at the DAΦNE electron-positron collider of the INFN National Laboratory of Frascati (INFN-LNF) in Italy, aiming to perform the first-ever measurement of the $2p \rightarrow 1s$ X-ray transitions in kaonic Deuterium, a crucial step towards determining the isospin-dependent antikaon-nucleon scattering lengths. Based on the experience gained with the previous SIDDHARTA experiment, which performed the most precise measurement of the kaonic Hydrogen $2p \rightarrow 1s$ X-ray transitions, the present apparatus has been upgraded with innovative X-Ray Silicon Drift Detectors (SDDs), distributed around a cryogenic gaseous target placed in a vacuum chamber at a short distance above the interaction region of the collider, two new veto systems and a charged kaon detector. The current work presents a comprehensive description of the SIDDHARTA-2 setup, including the optimization of its various components during the commissioning phase of the collider.

Keywords: Detector control systems (detector and experiment monitoring and slow-control systems, architecture, hardware, algorithms, databases); Instrumentation for particle accelerators and storage rings - low energy (linear accelerators, cyclotrons, electrostatic accelerators); Photon detectors for UV, visible and IR photons (solid-state) (PIN diodes, APDs, Si-PMTs, G-APDs, CCDs, EBCCDs, EMCCDs, CMOS imagers, etc); X-ray detectors

*This article is dedicated to the memory of Carlo Guaraldo, with whom many of us shared a long and rewarding journey through the field of strangeness physics.*

2024 JINST 19 P11006

## Contents


**1 Introduction** **1**

**2 Experimental requirements for the kaonic deuterium measurement** **2**

**3 The SIDDHARTA-2 setup** **2**

3.1 The setup vacuum chamber, the calibration system and the shielding 3

3.2 The beam pipe and the Mylar degrader 4

3.3 Kaon trigger detector and luminosity monitor 5

3.4 The cryogenic target cell 9

3.5 The SDD detector system 10

3.6 The veto detector systems 12

3.7 The trigger logic and the data acquisition system 19

**4 Conclusions** **21**


## 1 Introduction

The X-ray spectroscopy of light kaonic atoms is a unique tool for investigating Quantum Chromodynamics (QCD) in the low-energy strangeness sector. Precise measurements of the radiative X-ray transitions towards low-n levels in these exotic systems provide information on the kaon-nucleus interaction at threshold which, until now, was inferred by extrapolating towards zero energy the results of scattering experiments at larger momenta, making it method-dependent.

The electromagnetic (EM) interaction of kaons with the nucleus is well described by Quantum Electrodynamics (QED) and the energy levels can be calculated with eV precision by solving the Klein-Gordon equation. Given the reduced size of the kaonic atom in its lower states, allowing for the action of the nuclear forces, the deviation of the transition energy to these levels from the electromagnetic value and the increased line width provide information on the strong interaction between the kaon and the nucleus. Therefore, the observables of interest are the shift ($\epsilon$) and the width ($\Gamma$) of the transitions to the lowest reachable levels, directly related to the shift and the width of the last, induced by the strong interaction [1]. Due to the large kaon mass, the transitions are in the X-ray range.

A special role is played by the lightest kaonic atoms, namely kaonic Hydrogen, Deuterium, and Helium. From the first two, the isospin-dependent antikaon-nucleon scattering lengths can be extracted by using the Deser-Truman formalism including three-body and isospin correction. Additional information on many-body strong interaction can be retrieved from the transitions in kaonic Helium. The kaonic Hydrogen strong interaction-induced 1 s level shift and width have been measured by the KpX experiment (E228) at KEK [2] and by the SIDDHARTA experiment at DA$\Phi$NE in 2009 [3], while the first kaonic Deuterium measurement is in progress at the DA$\Phi$NE collider by the SIDDHARTA-2 collaboration.

SIDDHARTA-2 apparatus has been developed to address its objective, facing two challenging issues: a very small estimated X-ray yield and a huge electromagnetic and hadronic background [4].

2024 JINST 19 P11006

The experiment aims performing the kaonic Deuterium measurement with a similar precision as the one of kaonic Hydrogen, namely 30 eV for the shift and 70 eV for the width. The results, coupled with the existing kaonic hydrogen data, allow obtaining the antikaon-nucleon isospin 0 and 1 scattering lengths, which are fundamental quantities for understanding the non-perturbative regime of the strong interaction in the presence of strangeness. The aimed accuracy is essential to efficiently disentangle between different theoretical approaches [5–9].

The following section describes the experimental requirements for kaonic deuterium measurements. In section 3 a detailed description of the apparatus is given, comprising the optimization of various components, while the conclusions are presented in section 4.

## 2 Experimental requirements for the kaonic deuterium measurement

The DAΦNE accelerator complex is a double-ring electron-positron collider, operating at the center of mass energy of the $\phi(1020)$. The back-to-back $K^+K^-$ pairs, produced in the subsequent $\phi$-decay with a $\simeq$ 49% branching ratio [10], exhibit a low momentum ($\simeq$ 127 MeV/c) and a low energy spread ($\delta p/p \simeq 0.1\%$), making this machine an ideal environment for precision spectroscopy of kaonic atoms. DAΦNE attained its maximum luminosity after implementing an innovative Crab-Waist collision scheme with the SIDDHARTA apparatus in 2009, achieving a peak luminosity of $4.5 \times 10^{32}\,\mathrm{cm}^{-2}\mathrm{s}^{-1}$ [11]. As stated, the experimental challenge is related to the very low kaonic deuterium X-ray yield, estimated in the $10^{-3}$% range, one order of magnitude below the kaonic hydrogen one, the larger lines width, impacting the signal-to-background ratio (S/B), and the difficulty to perform precision X-ray spectroscopy in the high radiation environment of the near vicinity of the collider interaction point (IP). The key requirements were defined using a GEANT4 Monte Carlo (MC) simulation implementing in a realistic manner the setup configuration, the hadronic processes subsequent to the $\phi(1020)$ decay as well as the accelerator background, consisting mainly in Touschek (in-bunch elastic scattering resulting in momentum variation beyond the dynamic acceptance in bendings) and beam-gas induced EM cascades, developing in the nearby collider elements (quadrupoles, beam pipe, etc.). As a result, a new generation of faster, large area X-ray SDD detectors with good energy (FWHM $\simeq$ 150 eV at 6.4 keV) and timing (500 ns FWHM) resolutions operating in a stable manner under the high accelerator background were needed and subsequently developed inside the collaboration, together with two veto systems and a charge identification detector operating without a magnetic field, all concurring in improving the S/B by about one order of magnitude compared to the kaonic hydrogen measurement performed by SIDDHARTA. A cryogenic light-weight gaseous target operated at 20 K optimizes the kaons stopping efficiency by reaching the required density at relatively low pressure ($\sim$ 1.5 bar) so avoiding using thick, X-ray absorbing walls. The system implementation is described in the following section.

## 3 The SIDDHARTA-2 setup

The SIDDHARTA-2 setup was mounted in the interaction region (IR1) of the DAΦNE collider in 2019. The low-momentum negatively charged kaons from $\phi(1020)$ meson decay pass through the lightweight C-Al beam pipe, are further slowed down by a Mylar degrader, then stopped in the gaseous target placed at a short distance (12 cm) above the IP, forming kaonic atoms. The X-rays



2024 JINST 19 P11006

produced by the de-excitation of the lasts are detected by the surrounding SDDs. A sketch of the apparatus is shown in figure 1.

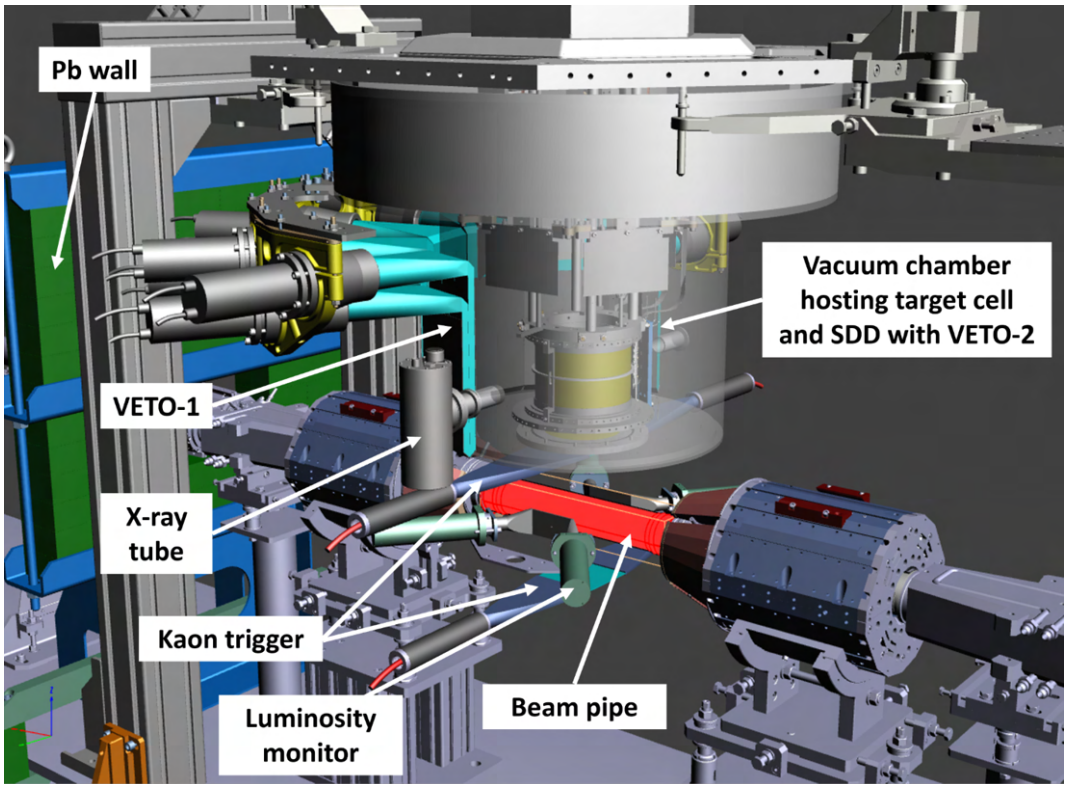


**Figure 1.** Schematic view of the SIDDHARTA-2 apparatus installed on the IR1 of the DAΦNE collider. The main components are the beam pipe, the kaon trigger, the cylindrical vacuum chamber containing the cryogenic target surrounded by the X-ray detectors (SDDs), the veto systems and the luminosity monitor. The lead table, the second lead wall are not shown in this figure to keep the other elements of the setup visible.

A lead table and two lead walls complete the structures to shield the apparatus from particles, mostly Minimum Ionizing Particles (MIPs), lost from the $e^+e^-$ rings. The components of the apparatus are described in more detail in the following subsections. The last component of the veto system, the $K^-$ Veto detector, was inserted after the installation of the main elements of the setup and is described in section 3.6.

### 3.1 The setup vacuum chamber, the calibration system and the shielding

A turbo-molecular pump and an oil-free isolated dry scroll pump work in cascade, attached to the target and SDDs vacuum chamber and providing a flow of 300 l/s, needed for reaching the insulation vacuum for cryogenics, below $10^{-6}$ mbar. A system composed of two X-ray tubes operated at 50 kV are responsible for the periodic calibration of the SDDs, by exciting the X-ray fluorescence of high-purity Titanium and Copper foils mounted on dedicated frames on the target walls. A 6 cm thick lead platform and two lateral lead walls 10 cm wide act as supporting and shielding structure. The shielding is required to protect the setup against the large flux of particles lost from the $e^+e^-$ rings via the Touschek effect and beam-gas interaction, developing electromagnetic cascades and creating background on the SDD detectors.



2024 JINST 19 P11006

### 3.2 The beam pipe and the Mylar degrader

The kaons exiting the collider IP cross a low material budget cylindrical beam pipe, made of 150 µm thick aluminum layer with an internal diameter of 58 mm and a length of 380 mm, reinforced by an outer layer of 500 µm carbon fiber (figure 2). The pipe ensures a minimal stopping of the low energy kaons, while maintaining the ultra-high vacuum required by the collider operation and the electric continuity of the accelerator rings, for minimal coupling impedance to the circulated beams. The beam pipe was soldered to the rings vacuum chamber, to avoid flanges which would develop additional EM showers near the setup entrance collimator. The bellows for compensating for thermal strain and the mechanical misalignment were installed outside the interaction region.

As the electron and positron beams cross at the IP with an angle of 50 mrad, the center of mass of the produced Φ meson receives a boost towards the center of the collider, subsequently reflected in the momentum distribution of the $K^+K^-$ pairs (figure 2). A step-wise Mylar degrader is placed in front of the kaon entrance window of the vacuum chamber to compensate for the effect while moderating the kaon momentum and obtaining a uniform stopping distribution of the lasts inside the cryogenic target.

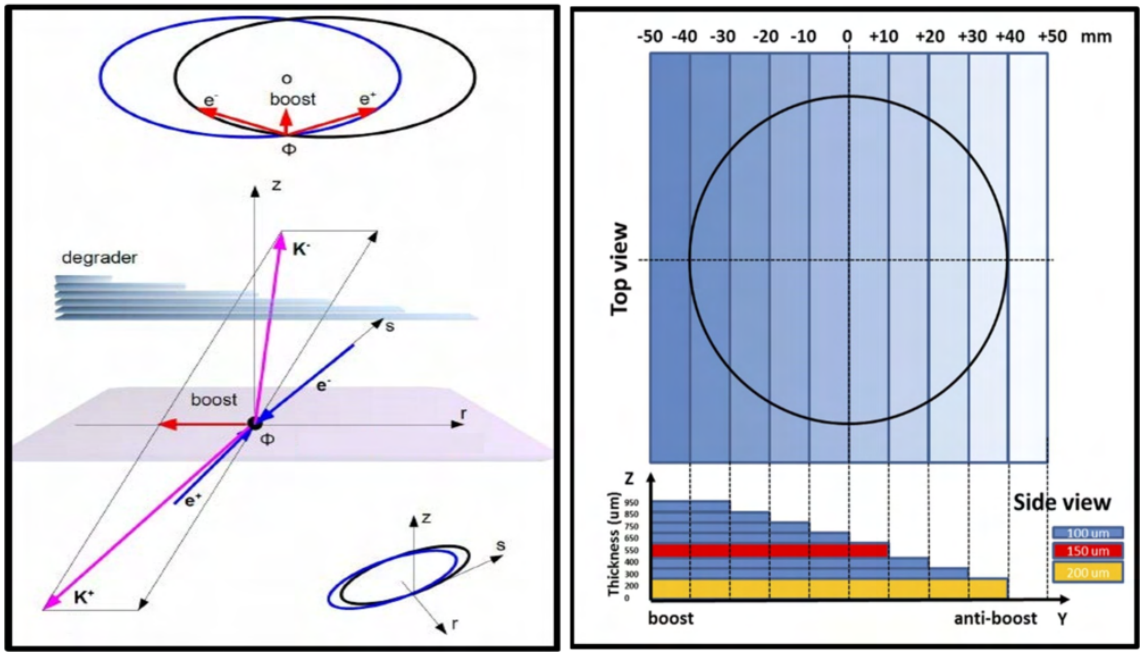


**Figure 2.** Left: a sketch of the electron and positron beams crossing under a small angle at the IP in DAΦNE, imparting a boost to the Φ meson and consequently, to its decay products; consequently, the degrader thickness is gradually increased to compensate the momentum variation of the kaons. Right: schematic drawing of the Mylar degraded. The circle represents the size of the entrance window of the vacuum chamber. The zero on the Y-axis corresponds to the IP. The degrader has 8 steps with different thicknesses to compensate the boost of the kaons. The middle thickness is the reference value and is reported in various figures to identify the various degraders. Reproduced from [26]. © The Author(s). Published by IOP Publishing Ltd. CC BY 4.0.

To optimize the shape and the thickness of the degrader, MC simulations have been performed, as well as an experimental fine-tuning based on the intensities of kaonic X-ray lines. For the kaonic Helium4 ($K^4$He) measurement, the number of $3d \rightarrow 2p$ transition events, normalized to the number of the triggered kaons and to the effective detection surface, was recorded for different degrader



2024 JINST 19 P11006

configurations. The resulting trend as a function of the degrader central thickness, taken as reference point, was compared with the MC predictions (figure 3). The slightly larger width of the measured optimization curve with respect to the MC one is due to the non-uniform density distribution of the carbon fiber and resin reinforcing the beam pipe, while the optimal value for maximizing the signal is in good agreement between the two, thus validating the MC also for targets were the signal is observed after long periods of acquisition, precluding a multiple degrader scan. The degrader tuning for each target is an important operation since even small deviations in the order of 100 µm can significantly reduce the kaonic atom signal as shown in the figure 3.

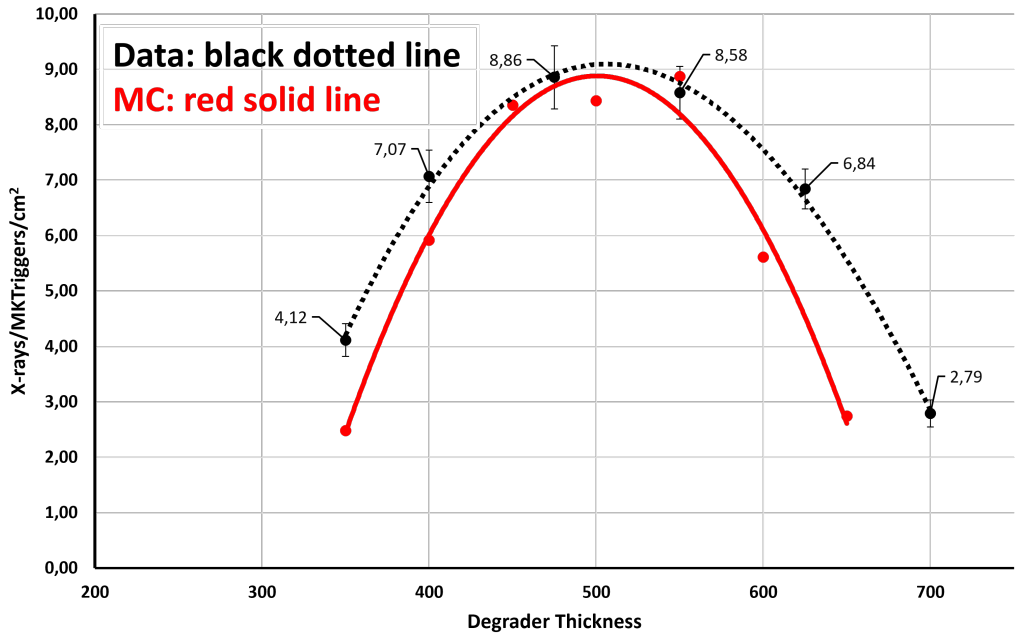


**Figure 3.** Degrader optimization curves: kaonic helium-4 ($K^4He$) $3d \rightarrow 2p$ signal normalized to the numbers of the triggered kaons and effective detection surface (black dotted line) vs. degrader thickness in µm (center values of the degraded as a reference point), together with the MC predictions (red solid line).

### 3.3 Kaon trigger detector and luminosity monitor

The trigger logic is essentially based on the back-to-back topology of the $K^+$ and $K^-$ tracks and on their large energy deposition in a thin scintillator, while the MIP's characteristic one is about one order of magnitude lower. Therefore, the kaon pairs are detected as coincident hits with two Scionix EJ-200 plastic scintillators with a size of $100 \times 100 \times 1.5\,mm^3$, mounted above and below the beam pipe, each read by two Hamamatsu R4998 Photo-Multiplier Tubes (PMTs), as shown in figure 4.

However, the above criteria for kaon selection proved to be insufficient as the EM showers from the 510 MeV lost electrons and positrons, developed along the beam pipe, hit the scintillators at grazing angles, releasing over the corresponding long path an amount of energy comparable to the transverse kaons; moreover, the extension of the showers allows them to hit both scintillators, producing coincidence events.

Therefore, a third criteria, related to the slow kaons time-of-flight (TOF) was introduced, allowing distinguishing them from the fast MIPs or other fast $\phi(1020)$ decay products. As no $\phi$ production/decay



2024 JINST 19 P11006

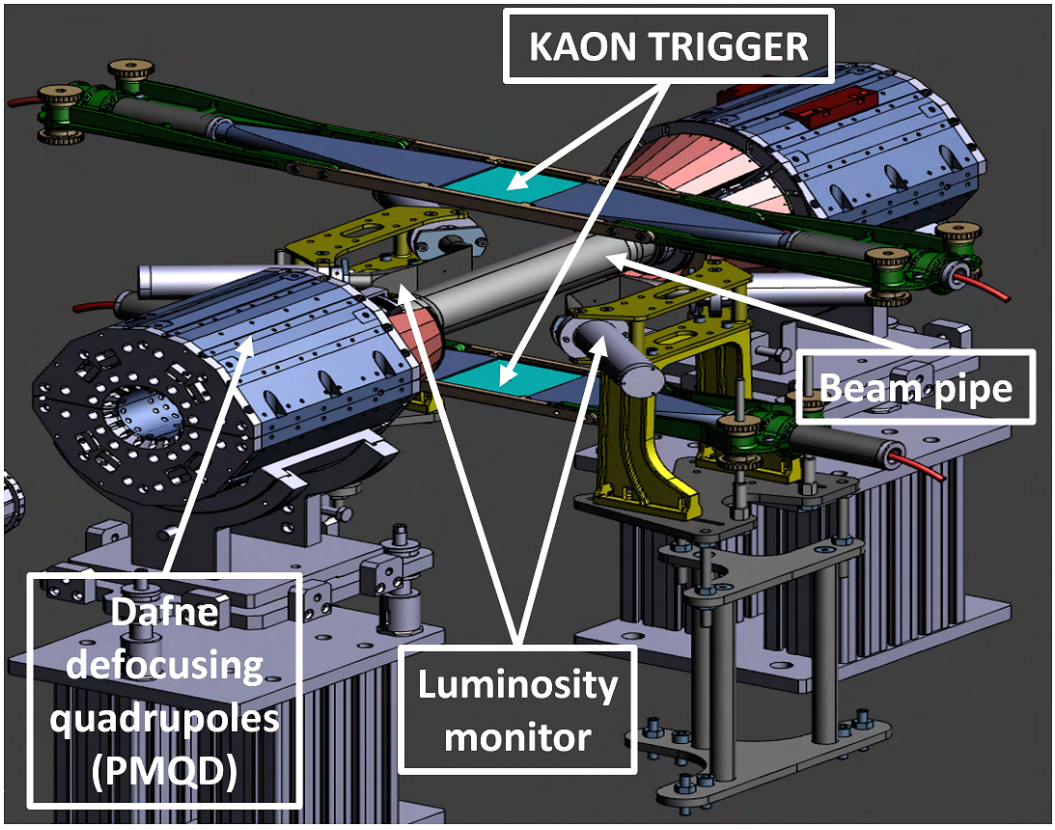


**Figure 4.** Schematic layout of the kaon trigger detector placed in the vertical plane and the luminosity monitor on the horizontal plane of the IP.

prompt can be extracted, the collider radiofrequency (RF $\simeq$ 368 MHz), synchronous with the bunches and therefore, with their crossing, was used as clock signal. The EM showers reach the scintillators with a delay lower than 100 ps with respect to their originating bunch; the same is valid for the fast pions from the $\rho\pi^+$, $\pi^+$, $\pi^-$, $\pi^0$, $\phi$ decay channel, while the kaons need about 1.2 ns to reach them. By measuring the time between a coincidence and the successive RF pulse one can extract, to a constant offset, the bunch timing minus TOF, modulo bunch period (1/RF), providing a good separation between kaons and MIPs. Moreover, applying the method on the bi-dimensional plot of the two TOF corresponding to the two scintillators, the residual MIPs tail contamination is reduced to negligible levels. In practice, as most NIM modules do not respond to the 368 MHz RF frequency, the lower harmonic (RF/2) was used, thus splitting the distribution in two peaks for kaons and two for MIPS, without any impact on selection (figure 5). The 4 PMT-RF signals, processed by Constant Fraction Discriminators (CFD) are acquired by 4 multi-hit TDC channels and the spectrum is built for the mean time of each scintillator. The selection of coincident kaons and MIPS is done offline, while the hardware trigger signal is provided only by the coincidence, after a relatively high CFD threshold (placed just below the kaon energy deposition charge-equivalent), rejects a large fraction of MIPs. The selection of triggered X-ray events grants a background reduction factor (defined as the ratio between the number of events with a trigger and the overall X-ray in the ROI) of $10^5$, without which the signals from kaonic atoms would be impossible to observe. Further reductions are obtained when rejecting the coincident MIPS hitting the KT and applying the veto systems described below.



2024 JINST 19 P11006

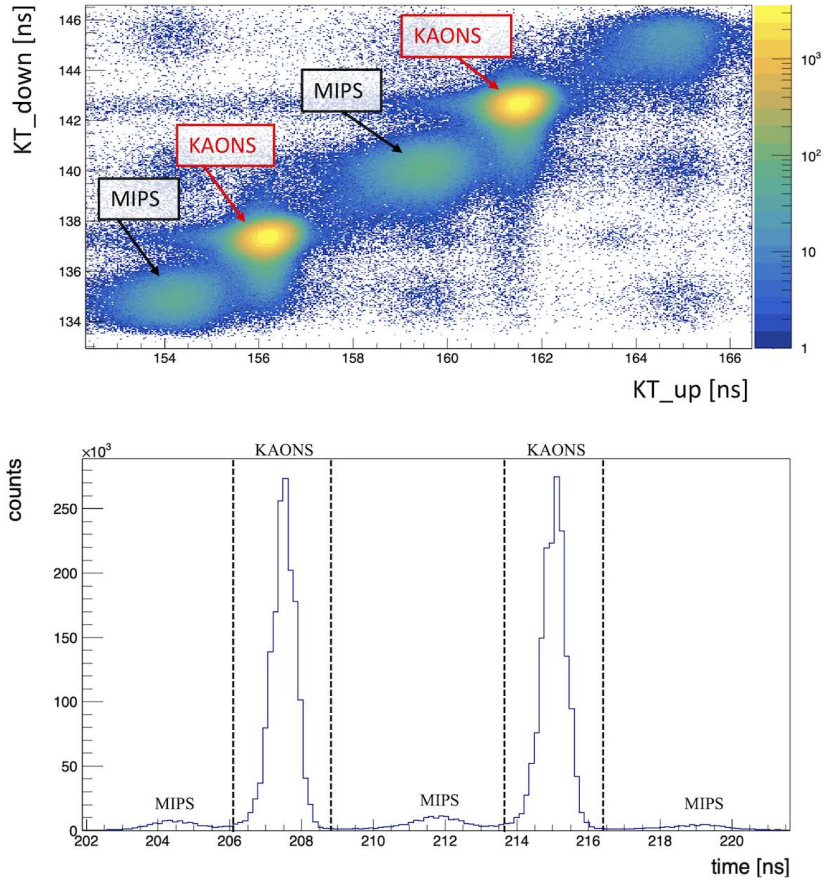


**Figure 5.** Time distribution of the up and down scintillators of the kaon trigger (top-panel), and its projection on the diagonal (bottom-panel). The coincidence events related to kaons (high intensity) are clearly distinguishable from MIPs (low intensity). The double kaon and MIPs structures are due to the use of DAΦNE RF/2 as time reference. Reproduced from [26]. © The Author(s). Published by IOP Publishing Ltd. CC BY 4.0.

The luminosity monitor detector is an instrument similar to the kaon trigger, placed in the horizontal plane of the accelerator rings, therefore not tagging the kaons entering the target. This detector is used to monitor the beam quality and background level in real-time, via ToF measurements of the kaons and MIPs produced by the collider. As the main machine background, related to Touschek losses, is spread on the horizontal plane (the reason for which the setup positioning was chosen in vertical), the luminosity monitor provides an additional kaon rate monitoring and a very fast assessment of the background conditions, for which the kaon trigger is less sensitive, being protected by placement and shielding.

The monitor consists of two parallel detection modules located on the opposite sides of the beam pipe, in the collider plane, corresponding to the $\phi$ boost and anti-boost directions, at a distance of 7.2 cm from the IP. Each module features an $80 \times 40 \times 2\,\mathrm{mm}^3$ BC-408 plastic scintillator, from Saint-Gobain Crystals, coupled at both ends to fast R4998 Hamamatsu PMTs through 6 cm fish-tail plastic light guides, glued at an angle of 38 degrees to fulfill the geometrical constraints of the apparatus [12]. The luminosity measurement is an important diagnostic tool for optimizing the collider performance. A dedicated data acquisition (DAQ) system computes the instantaneous luminosity based on the kaon



2024 JINST 19 P11006

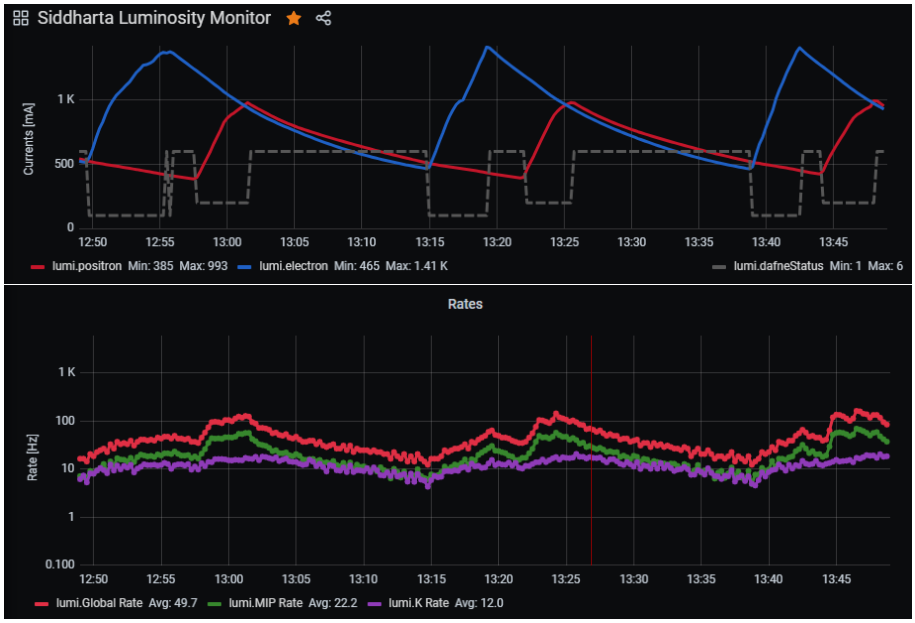


**Figure 6.** One hour record of the beam parameters during the kaonic helium data taking on 6 May 2023. On top part: red line — positron and blue line — electron beam currents, dashed line — the status of the accelerator; on bottom part: overall coincidence rates — red line, counting rates for online selected kaons — green line and MIPs — magenta line as recorded by the luminosity monitor.

coincidence rate normalized with the efficiency factor calculated by Monte Carlo simulation. The collection time interval has been fixed to 15 s, to ensure accuracy of a few percent of the measurement when the luminosity ranges between $0.5 \times 10^{31}$ cm$^{-2}$s$^{-1}$ and $20 \times 10^{31}$ cm$^{-2}$s$^{-1}$.

The luminosity monitor data, together with the SDDs and kaon trigger rates are feed in real time to the accelerator control system, allowing fine-tuning during operation and long-term performance recording. A web application connects the various beam indicators and the SIDDHARTA-2 control parameters under a Grafana@ graphical system, allowing multi-console monitoring. A screenshot of the web monitor interface is presented as an example in figure 6, whose central panel shows the diagnostic behavior of the colliding beams. The application tracks beam currents, coincidence rates between the two scintillators, counting rates for online selected kaons and MIPs and estimated instantaneous luminosity, the last shown in figure 7.

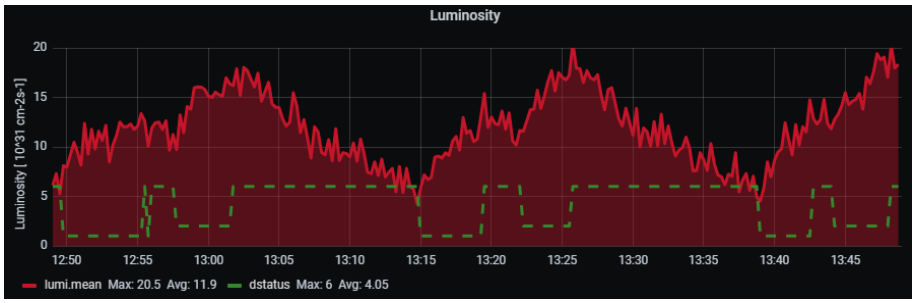


**Figure 7.** The estimated instantaneous luminosity, in units of $10^{31}$ cm$^{-2}$s$^{-1}$, for one hour of the kaonic helium data on 6 May 2023. The dashed green line marks the run status of the accelerator in the same period.



2024 JINST 19 P11006

### 3.4 The cryogenic target cell

There are strict requirements for the design of kaonic atoms target cell, like high-purity gas target systems, to avoid the Stark effect, cooled to cryogenic temperature to increase the density and consequently the number of kaons stopped in the gas. The behavior of a kaonic atom in a high density gas is strongly influenced by collisional effects. During the last steps of atomic deexcitation cascade, the very small atom size on the lower levels, related to the large kaon mass, makes it behave as a neutral particle, thus overcoming the electrostatic barrier when colliding with other atoms and accessing the high electric field region of their nuclei. This induces Stark mixing with successive kaon absorption from levels above the fundamental one and, consequently, a strong drop of the yield of the transition of interest to the 1 s level, in the case of kaonic deuterium. As the yield is inversely dependent on density, on the other hand, a too low density implies long moderation times and kaon decay, as well as low stopping and detection efficiency. Hence, some cascade calculations [13], coupled with Monte Carlo efficiency estimates give important indications for the optimal density to be used in a specific configuration.

As a result, the target working point is set as the best compromise between the kaons stopping efficiency, detection efficiency, kaon moderation and decay and the Stark mixing. In the case of SIDDHARTA-2, the optimized value for Deuterium is about 1.5% liquid density, which cannot be obtained only by increasing the pressure, due to the strong absorption of the X-rays by high pressure, thick walls in front of detectors, as well as the stopping of kaons in the entrance window. Thus, a light target operating at low temperature is required for maximizing the overall signal.

The SIDDHARTA-2 cryogenic target is a cylindrical cell with a diameter of 144 mm and a height of 125 mm. The side wall is made of two layers of 75 µm Kapton@ film, ($C_{22}H_{10}N_2O_5$), with a reinforcement structure made of high purity aluminum (figure 8). The kaon entrance window is made out of 125 µm thick Kapton@ foil, alternated with a similar thickness Mylar, according to the target gas filling, while the internal part of the top aluminum ring is covered by a 100 µm Ti layer for continuous in-situ calibration purposes, using the beam fluorescence activation (PIXE), in addition to the Ti and Cu periodic calibration described above. The cooling and mounting structure of the target is installed on the top side and is shared with the SDD detectors, as shown in figure 8.

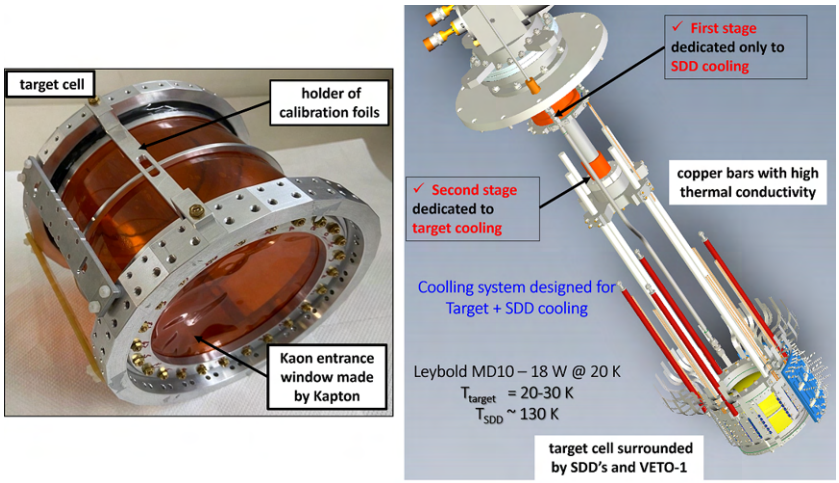


**Figure 8.** Left: foto of the SIDDHARTA-2 cryogenic target cell made of Kapton walls. Right: schematic layout of the cooling system for the SDD arrays and target cell.



2024 JINST 19 P11006

A closed-cycle helium refrigeration system is used to keep the target cell between 20 K and 30 K with a maximum pressure of 2 bar. The cryogenic refrigeration system comprises the compressor unit (COOLPAK 6000-1) and a two-stage cold head (model COOLPOWER 10 MD) connected with flex lines. The first stage of the cold head provides higher cooling power and operates at higher temperatures (115 W at 80 K), matching perfectly the SDD detector's cooling demands, related to the electronic noise, the charge mobility, and the thermal load of the on-board buffers and connections. The second stage, delivering lower power at a much lower temperature (18 W at 20 K) is attached to the target, which has no other thermal contacts and is insulated by the vacuum and a set of super-insulation aluminized Mylar foils, 7 µm thick, wrapped around and below. A PID-controlled heating system was installed on the target and on the SDDs, allowing operating it at different stable temperatures and pressures, depending on the employed gas.

### 3.5 The SDD detector system

The Silicon Drift Detectors (SDDs) were first proposed by E. Gatti and P. Rehak in 1984 [14]. The basic idea of the side-ward depletion, the revolutionary concept at the basis of the SDD and of the related devices, is to fully deplete the semiconductor substrate through a point-like "virtual contact", as the anode is called in the original paper. The key feature of SDDs, with respect to a conventional PIN diode of equivalent active area and thickness, is its extremely low readout capacitance (100 fF). This is determined by the small n+ anode area and is essentially independent on the detector size, a crucial improvement for minimizing the capacitive noise as compared to PIN photodiodes. Therefore, optimal energy resolution (mainly limited by the Fano "noise") can in principle be achieved also for large-area detectors. A further improvement comes from the shape, the SDD having a set of concentric p+ rings surrounding the anode on one side and a large continuous p+ electrode on the opposite side. Since the detectors for spectroscopy are intended to measure only the energy and not the interaction point of the incident radiation, the drift field is designed to have azimuthal symmetry due to the concentric drift rings. The potential gradient applied on the upper side sets the drift field for electrons, while the potential on the continuous back-plane guarantees the full depletion also in the anode region. The electrons released anywhere within the detector active volume are separated from the holes by the electric field and collected at the anode (figure 9). The backplane is realized with a uniform p+ implant which acts as a thin entrance window for the radiation.

Dedicated large-area monolithic SDD arrays have been developed by Fondazione Bruno Kessler for the SIDDHARTA-2 experiment. The silicon wafer is glued on an alumina board which provides the polarization to the units. The charges generated by the X-ray photoelectric absorption in the silicon are collected by the point-like central anode and amplified through a closely-bonded CMOS low-noise, charge-sensitive pre-amplifier (CUBE) [15]. The preamplifier has been designed to render the device performance independent from signal connection and to increase its stability, even when exposed to high charged particle rates generated by the collider operations. Moreover, the CMOS solution allows operating the device at a lower cryogenic temperature than the integrated J-FET pre-amplification stage previously used by SIDDHARTA, thus obtaining faster drift times (higher mobility) and therefore, higher time resolution, crucial for rejecting the asynchronous (with respect to the kaons) accelerator background. In practice, the SDD temperature lowered from 150 K to 130 K which, together with the new array geometry with smaller cell size (8 mm vs 10 mm), improved their time resolution by a factor 2, from 1 µs to 500 ns.



2024 JINST 19 P11006

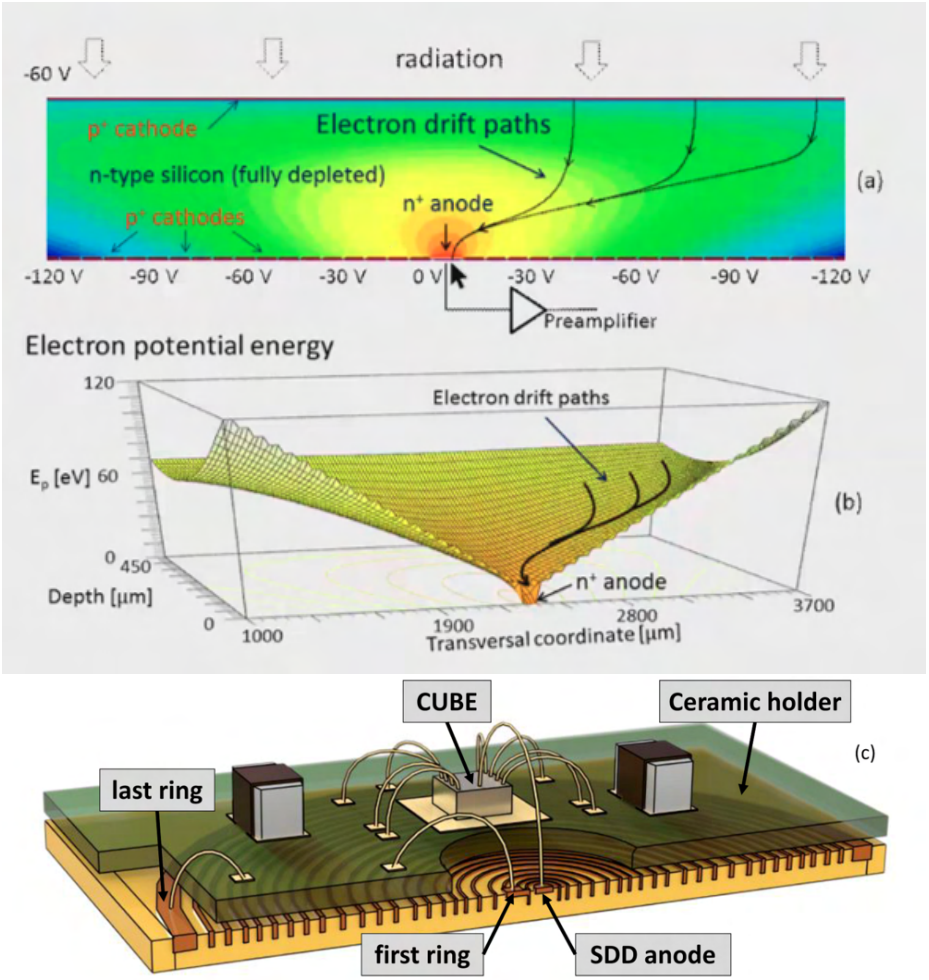


**Figure 9.** The drift field is represented as a color map (a) and the associated potential (b) is determined by the voltage applied to the divider, for an SDD with a uniform entrance window. The charge collection to the anode is indicated by the electron drift paths. A schematic layout (c) of the CUBE pre-amplifier mounted on the ceramic holder of the SDD.

Each 450 µm thick silicon array consists of 8 single cells arranged in a $2 \times 4$ matrix, with a total size of $34 \times 18\,\mathrm{mm}^2$ (including dead areas). The design of the array and of the carrier has been optimized in order to maximize the total active area of $5.12\,\mathrm{cm}^2$, as shown in figure 10.

The output lines of the CUBE pre-amplifiers are connected to a common ASIC, called SFERA (SDDs Front-End Readout ASIC), an integrated circuit performing analog shaping and peak detection of the signals [16, 17]. The SFERA main shapers feature a $9^{\mathrm{th}}$ order semi-Gaussian complex-conjugate poles filters with selectable peaking times (from 500 ns to 6 µs) and gain, while the fast shapers have a fixed 200 ns peaking time and are used for pile-up rejection. Each ASIC handles the signals produced by 16 SDD units (2 arrays) and provides the DAQ chain with the individual amplitude, address and hit timing information. The spectroscopic performance of the system has been optimized in laboratory [18] and tested during the beam commissioning phase of DAΦNE in early 2020, showing very good energy resolution of $157.8 \pm 0.3^{+0.2}_{-0.2}$ eV at 6.4 keV and a linearity at the level of 2 eV [19] in the region of interest (ROI) from 4 keV to 12 keV.



2024 JINST 19 P11006

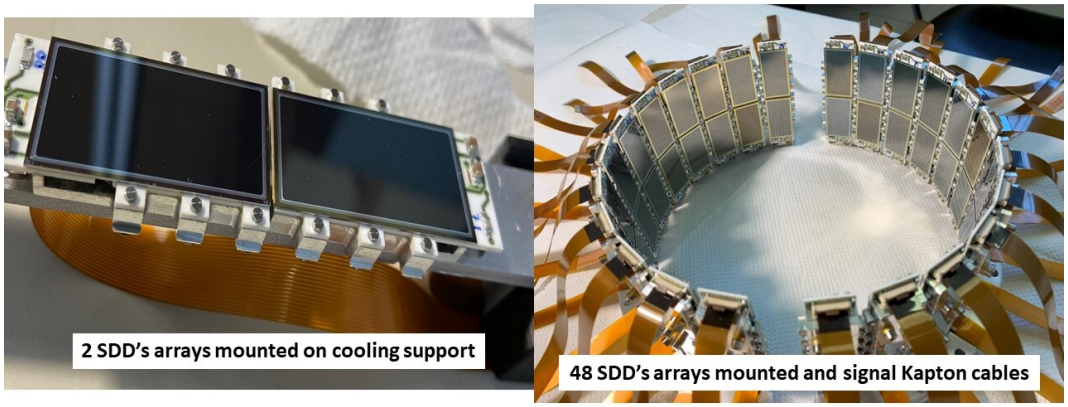


**Figure 10.** Left: the two SDD arrays mounted on the cooling holder. Right: all 48 SDD arrays are ready to be mounted around the target.

### 3.6 The veto detector systems

The measurement of kaonic deuterium transitions implies dealing with a low X-ray signal distributed over broad spectral lines and with a significant hadronic and electromagnetic background. After the main event selection, based on the kaon trigger described above, successive signal filtering is required to achieve the order of magnitude improvement over the previous measurements, imposed by the low kaonic deuterium yield. Three new detectors, shown in figure 11 were therefore introduced as veto systems for selecting gas-stopping events, for rejecting the MIPS depositing an energy in the

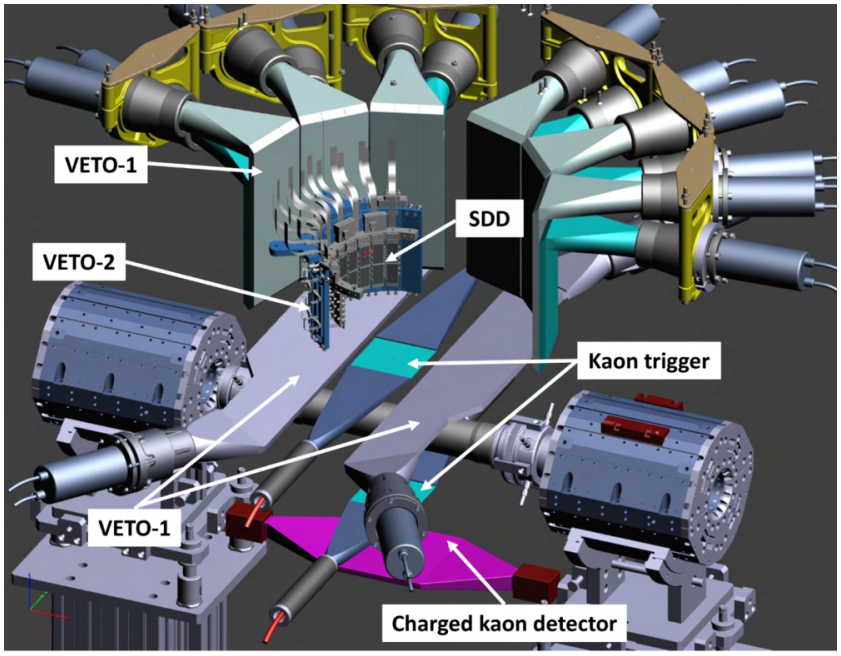


**Figure 11.** Schematic view of the veto systems installed in SIDDHARTA-2. Veto-1 is made out of scintillators slabs surrounding the vacuum chamber and two additional scintillators placed below it, at the sides of the kaon trigger. Veto-2 is an inner cylinder of plastic scintillation tiles, each placed at a short distance behind one SDD array. The $K^-$ detector (magenta) is located under the lower kaon trigger scintillator.



2024 JINST 19 P11006

same range as the X-ray signal of interest and for identifying the negative kaons in the trigger pairs when hitting the lower scintillator (opposite to the target).

The Veto-1 detector is a large solid angle scintillator barrel placed around and below the vacuum chamber which measures the timing of secondaries produced after the kaon absorption on the nuclei.

### 3.6.1 The Veto-1 system

For selecting the events occurring in the target, the relatively long $K^-$ moderation time in gas can be exploited. The time elapsed between the $K^-$ entrance in the target and its subsequent stopping and capture by a nucleus has a typical range from 3 to 7 ns, while the events involving a $K^-$ that stops in the solid components of the apparatus have a shorter characteristic time.

From the experimental point of view, this distinction requires measuring the arrival time of the fast charged secondaries emitted as consequence of the kaon nuclear absorption. The technique takes advantage of the high probability of production of at least one charged pion after the $K^-$ absorption [10].

Given that energetic secondaries from nuclear absorption easily pass through the SDDs and the vacuum chamber, the Veto-1 was placed outside the cylindrical vacuum chamber, allowing the installation of high efficiency light collection optics. The barrel is made of 12 distinct $(260 \times 110 \times 10)$ mm$^3$ plastic scintillator (ELJEN TECHNOLOGY, EJ-200) each one segmented into 3 equal strips to reduce the spread of the light paths and read out at both ends by two Hamamatsu R10533 PMTs through a complex multi-reflection light guides fitting the narrow space between the vacuum chamber and the external lead shielding (figure 12).

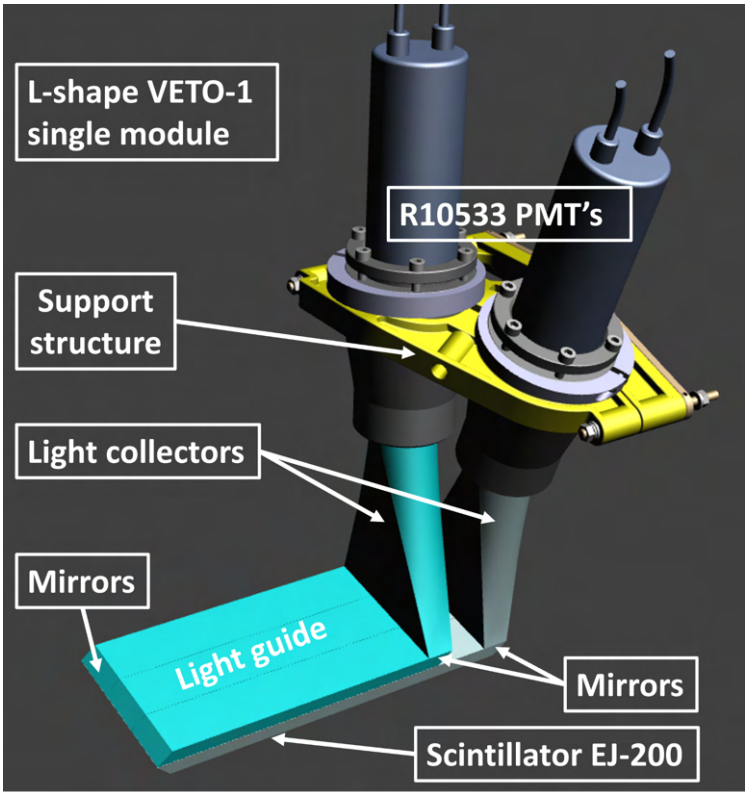


**Figure 12.** The Veto-1 layout for single module. The L-shape design is required due to small available space, involving mirrors to connect the scintillators and the light guides.



2024 JINST 19 P11006

The figure 13 shows the GEANT4 simulated time spectrum as provided by the Veto-1 system. The events inside the gas are characterized by a long $K^-$ moderation time. The main peak, centered at 5 ns after the $\Phi$ decay, corresponds to the arrival time of charged pions produced by the $K^-$ absorption by a gas nucleus, the "shoulder peak" below 3 ns is related to negative kaons stopped in the solid components of the setup (the dashed line in figure 13 represents the separation of the two regions: solid (left) and gaseous (right) material), while the long tail to the right is related to the $K^+$ decay. Hence, the Veto-1 time resolution must be below 1 ns to resolve the two peaks. A prototype was tested at the PSI (PiM1Muse line) with 170 MeV/c momentum pion beam showing a time resolution of 746 ± 53 ps FWHM and a detection efficiency of 96 ± 2% [20], in agreement with the requirements for SIDDHARTA-2 data taking campaign.

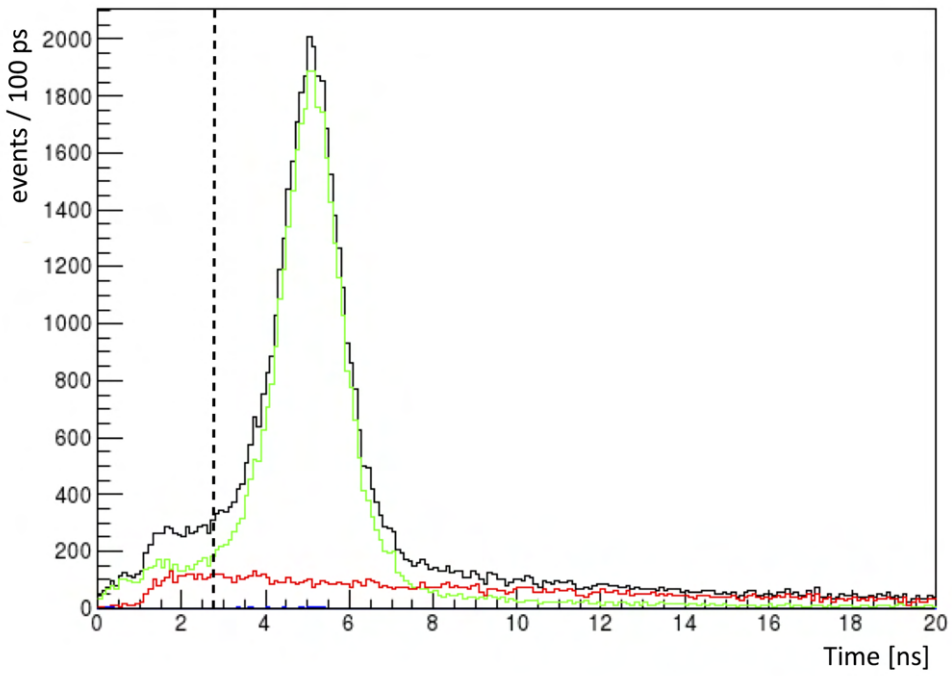


**Figure 13.** GEANT4 simulated time spectrum for the Veto-1 system. The main peak corresponds to particles produced by the $K^-$ absorption by a gas nucleus, while the "shoulder peak" on the left of the dashed line corresponds to $K^-$ stopped in the solid elements of the setup. The dashed line, around 3 ns, represents the separation of the two regions: signal from kaons stop in solid material (left) and gaseous (right). The green and red curves correspond to $K^-$ nuclear absorption and $K^+$ decays, respectively. Reproduced from [20]. © 2013 IOP Publishing Ltd and Sissa Medialab srl. All rights reserved.

The full Veto-1 system was also tested at PSI displaying efficiencies above the prototypes one (98%), and improved time resolution, as well (650 ± 50 ps FWHM). The detector was installed in 2022 on the SIDDHARTA-2 setup and successive testing was performed with the rest of the apparatus during the commissioning run of the experiment, when the target cell was filled with helium. The figure 14 shows the overall Veto-1 time distribution and the one correlated with X-ray emitted by kaonic Helium-4. The first peak corresponds to particles produced by $K^-$ absorption in the solid elements of the apparatus, the second one is due to $K^-$ stopped in the helium-4 gas target, while the right tail is due to positive kaons decay.

2024 JINST 19 P11006

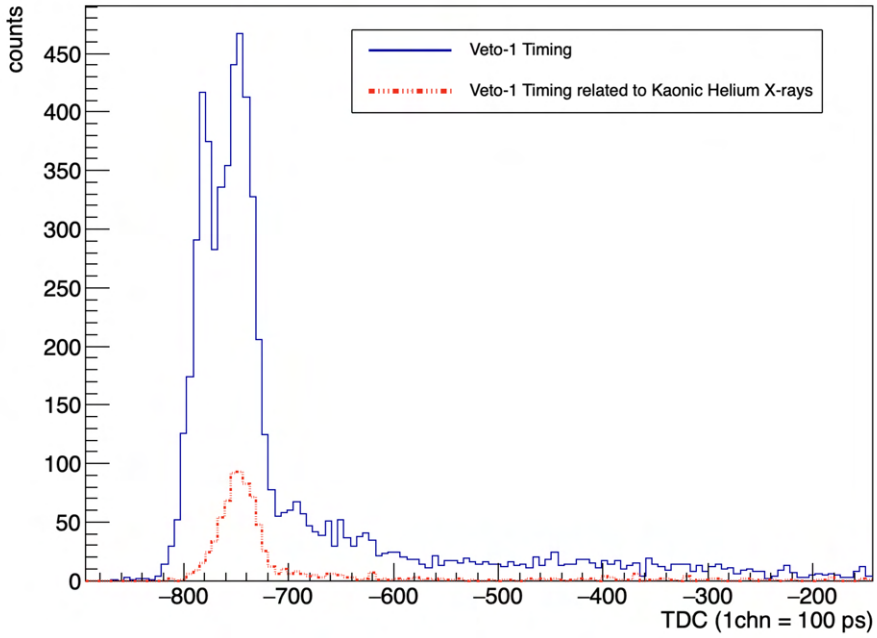


**Figure 14.** Veto-1 time distribution from TDC, measured during kaonic helium run. The red dotted line represents the time distribution of events corresponding to kaonic helium atoms.

### 3.6.2 The Veto-2 system

The negative kaons stopped inside the target undergo nuclear absorption and produce, besides the kaonic atom X-rays, several charged particles - mostly pions and protons - as well as neutrons and gamma rays. Their energy deposition in the SDDs depends on their path, as shown in figure 15. The charged particles that deliver signals in the SDDs in the same energy range as the relevant X-rays represent an important background source. The goal of the Veto-2 system is to suppress a fraction of this background, synchronous to the X-rays of interest. MIPs, back-scattered electrons and bremsstrahlung X-rays crossing the SDD on the edge of its active area deposit less energy than the ones passing through the full active depletion, thus producing a signal in the ROI. By using the spatial correlation between the SDDs and the corresponding Veto-2 scintillators placed behind each of them, part of these background sources can be eliminated.

The Veto-2 system consists of 24 units, each unit containing two plastic scintillators and four photodetectors, resulting in 96 read-out channels. Each scintillator ($50 \times 12 \times 5\,\mathrm{mm}^3$) is read out by two $4 \times 4$ mm Silicon Photomultipliers (SiPMs), manufactured by AdvanSiD. Optical grease and nylon screws couple the SiPMs to the scintillators [21]. A blue LED mounted on the print board between the SiPMs as shown in figure 16 provides calibration pulses.

The Veto-2 system has been tested and characterized at SMI, Vienna [22]. Though the main role of the detector is related to the topologic correlation with the SDD arrays, the average time resolution of $740 \pm 110$ ps FWHM enables the additional use of the timing information to distinguish between kaons stopped in the target gas and those ending up in the solid structures of the setup, in an analogous mode to the Veto-1 system. The intrinsic detection efficiency measured with cosmic rays was found to be $> 99\%$. The detector was installed behind the SDDs and tested during the kaonic helium data-taking period. The rejection of the signals produced by hadronic background



2024 JINST 19 P11006

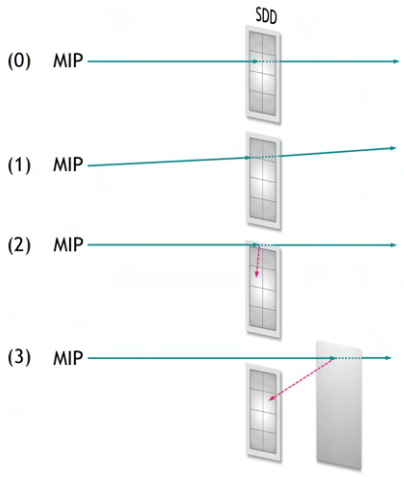


**Figure 15.** Typical events identified by the Veto-2 system: (Case 0) The MIP passes through the SDD's active center, producing a large signal outside the region of interest (ROI). (1) The MIP hits the SDD on the edge of its active area and a signal in the ROI can be produced. (2) Delta-rays hit the SDD. (3) Secondary X-rays or back-scattered electrons from the apparatus pass through the SDD. Reproduced from [23]. The Author(s). CC BY 4.0.

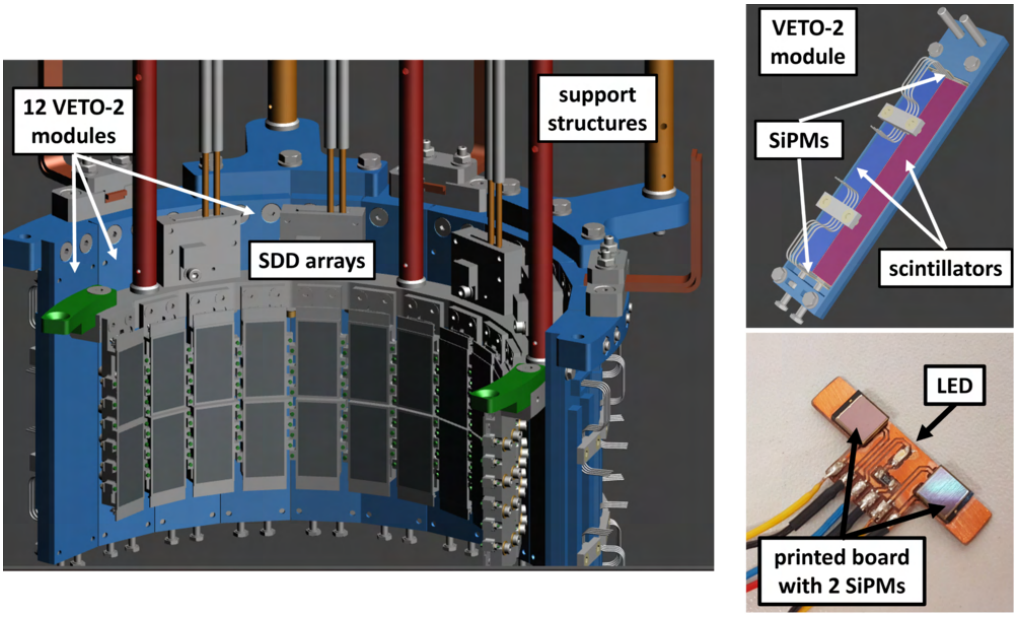


**Figure 16.** The Veto-2 system of SIDDHARTA-2. Left side: half of the total Veto-2 units placed behind the SDDs. Right side: a single unit with two scintillators and the corresponding PCB boards with two $4 \times 4$ mm SiPMs each; a calibration blue LED is mounted in the middle of each pair.

occurs when a coincidence between signals in the SDDs and the corresponding Veto-2 detectors is recorded (figure 17). The coincidence efficiency was found to be $62 \pm 1\%$ [23]. For the efficiency determination, SDD signals with energies $> 20$ keV were selected since they correspond to central MIP hits of the SDDs and thus produce signals in all detectors: the SDDs, the Veto-2, and the Veto-1. The efficiency was then determined as the ratio of total number of events in Veto-2 to the number of coincidences between SDDs and Veto-1 detectors.



2024 JINST 19 P11006

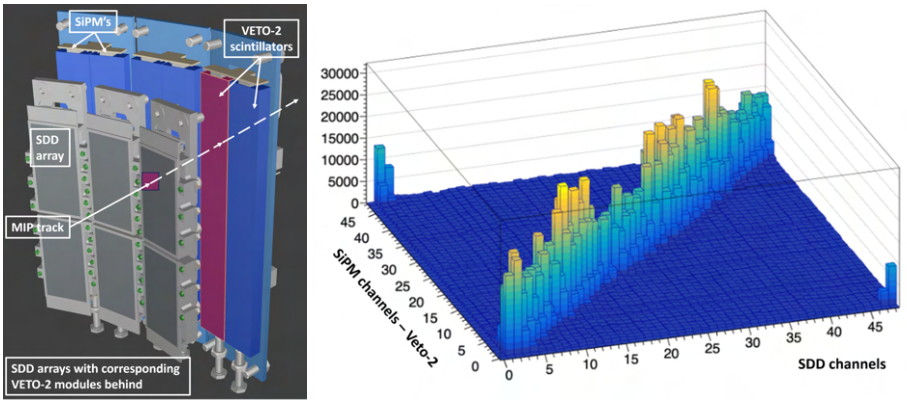


**Figure 17.** Topological correlation between hits in the SDDs and Veto-2. Left: track of a MIP crossing an SDD cell and the corresponding Veto-2 slab. Right: the event correlation between the SDD and Veto-2 channels during the kaonic helium test run.

The efficiency of the Veto-2 system within the SIDDHARTA-2 apparatus is lower than its intrinsic detection efficiency. This can be explained by an additional background component from beam-beam interactions along with the hadronic background component present during the measurement. The Veto-2 system not only actively suppresses the hadronic background, but it also is instrumental for the understanding of the background composition and the optimization of the machine and setup performances.

### 3.6.3 The $K^-$ Veto detector

As $K^-$ and $K^+$ are produced in pairs, 50% of the triggered events correspond to a positively charged kaon entering the target cell and producing background. Since the positive kaons decay with a characteristic time of 12.4 ns [10] without being bound and undergoing nuclear absorption, a fraction of them can be identified in the upper tail of the Veto-1 time spectrum recording the emitted muon, as stated above. For distinguishing the remaining (majority) of $K^+$, a third veto detector for the paired $K^-$ crossing the bottom slab of the kaon trigger was designed.

The main difficulty in identifying the kaon charge comes from the very short distance to the interaction point, required for efficient triggering and the subsequent short path traveled by the low momentum kaons crossing the trigger scintillator before they decay, both precluding the use of magnetic fields in a region near to the interaction point, were would impact on collider optics performance. After several Monte Carlo simulations and beam test runs of the kaon signal and of the subsequent secondaries indicated a reduced efficiency of pulse shape discrimination due to the dominant kaon energy deposition, a novel solution was adopted relying exclusively on secondaries after completely eliminating the kaons interaction with the sensitive detector, by stopping them in a passive Teflon layer lining the scintillator. The working principle is schematically shown in figure 19. After a $K^-$ is stopped in Teflon, it is quickly captured in an atomic orbit and subsequently absorbed by the nucleus, leading to the prompt emission of charged particles in less than 2 ns. As the majority of $K^-n/K^-p$ cases are characterized by multiple charged secondaries ([10]), the probability of one of them crossing the scintillator slab behind the Teflon stopper is $\sim$ 83%, even though only the $2\pi$ solid angle is covered. On the other hand, the $K^+$ undergoes a slow exponential decay, typically emitting a muon and an antineutrino and having a total prompt probability of $\sim$ 53%. Therefore, the hit time distribution of the secondary charged particles provides fairly good charge identification, especially in the case of $K^-$, as shown by the simulated



2024 JINST 19 P11006

response in figure 18, allowing rejecting its paired $K^+$ in the target. By combining this information with the additional direct $K^+$ identification by the Veto-1 detector described above, the overall efficiency of rejecting a triggered positive kaon is~ 90%, with consequent hadronic background suppression.

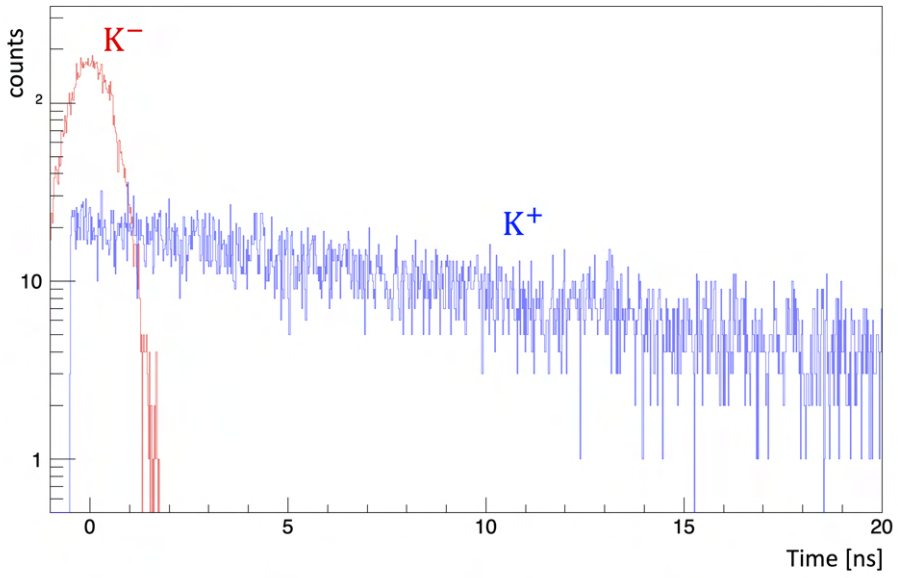


**Figure 18.** Simulation of the kaon charge detector time distribution. The $K^-$ and $K^+$ contributions are highlighted in red and blue, respectively. Reproduced with permission from [24].

The charge identification system, consisting in a $150 \times 150 \times 5\,mm^3$ plastic scintillator, read out by two PMTs and covered by a 3 mm Teflon@ layer, has been installed below the bottom scintillator of the Kaon Trigger (figure 11).

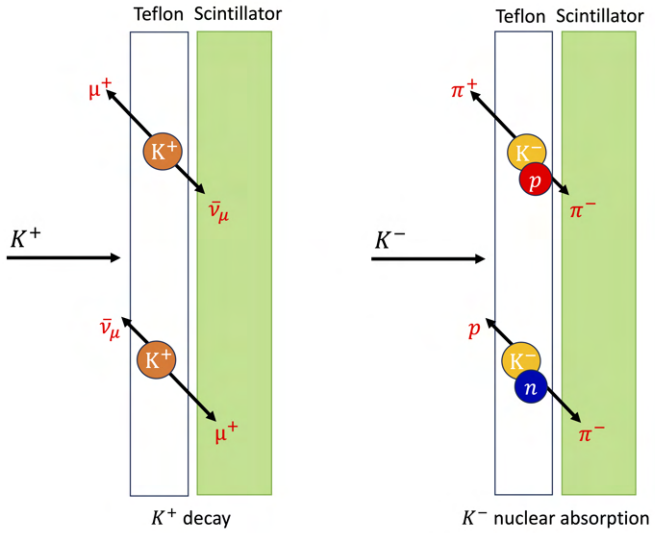


**Figure 19.** Schematic diagram showing the kaon charge detector functioning. The negative kaons stopped in Teflon get absorbed in a very short time (1–2 ns), typically releasing two fast charged secondaries, while the negative ones decay over longer time scale, emitting a positive muon and an antineutrino.

2024 JINST 19 P11006

### 3.7 The trigger logic and the data acquisition system

As stated, the trigger is generated by the coincidence between the signals of the upper and the lower KT scintillators. Most of the trigger pulses correspond to a back-to-back $K^+K^-$ pair, while the residual coincident MIPS from EM cascades depositing energy exceeding the kaon threshold (set on constant fraction discriminators) are identified and eliminated offline using the above-described ToF technique based on the collider RF. The timing of all scintillator channels (trigger and veto) is recorded with a multi-hit TDC (CAEN V1190A) taking the coincidence-gated RF/2 signal (bunch crossing) as reference.

The SDD real time signal (called "low threshold", LT) is recorded on a different chain, driven by an FPGA clock which measures the time difference between the trigger and the SDDs shapers peaks, precisely correlated with the anode charge collection. Given the relatively slow (500 ns) collection process with respect to the scintillators response, the FPGA clock, set at 120 MHz (8.33 ns period) provides a good enough timing accuracy. The SDD events are tagged with the trigger mark in a wide time window of 5 µs, to account for the delayed response of the shapers when saturated by MIPs and to allow background sampling, as well. The precise X-rays drift time selection inside the 500 ns window is performed offline. The time information provided by the SDDs was used to further reduce the electromagnetic background. The SDDs' timing resolution, which depends on the temperature, determines the acceptance window (Drift Time cut). Figure 20 shows the time difference between the kaon trigger signal and the X-ray hits on the SDDs (Drift Time) for the SIDDHARTA-2 runs. The rejection factors shown in table 1 refer to the data accumulated with the helium gas target for a total integrated luminosity of 76 $pb^{-1}$ [25] .

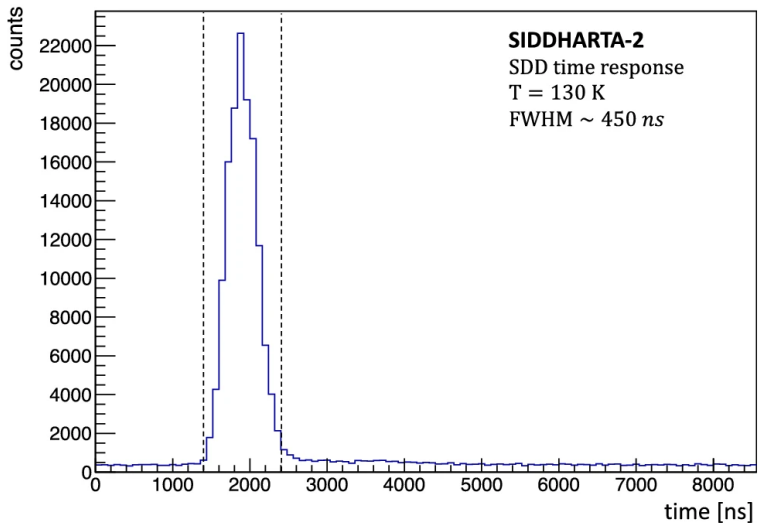


**Figure 20.** Distribution of the time difference between the SDD X-rays hit (LT) and the trigger signals during the SIDDHARTA-2 runs (sample of a few days of data taking for a total integrated luminosity of 76 $pb^{-1}$). The dashed lines represent the drift time window cut used to reduce the background obtained in offline analysis. Reproduced from [25], with permission from Springer Nature.

In conclusion, a valid SDD event is the result of a triple coincidence with two-time windows imposed during data analysis (trigger-RF and Drift Time-Trigger).

Any hit on one of the 384 SDDs and any kaon trigger generate a DAQ event, regardless if the two are correlated or not. The veto detectors are acquired only when a kaon trigger is present. This



2024 JINST 19 P11006

**Table 1.** Data selection steps to reduce the background together with the number of events passing each requirement and the associated background rejection factor are shown. Reproduced from [25], with permission from Springer Nature.

| **Selection** | **Events/pb$^{-1}$** | **Rejection factor** |
|---|---|---|
| No cut | $2.1 \cdot 10^7$ | // |
| Trigger cut | 1,560 | $1.3 \cdot 10^4$ |
| ToF cut | 1,032 | 1.5 |
| Drift time cut | 515 | 2.0 |

allows fully recording (and subsequently, subtracting) the machine background with high accuracy, controlling the event multiplicity and estimating the kaonic atom transition yields. The acquisition process for the scintillators (TDC) and SDDs (ADC, Drift time and address) is controlled by two FPGA boards operating a sparse DAQ algorithm in a master-slave configuration. Events within 5 µs are assigned the same event ID.

The SFERA ASIC provides an LT pulse for each SDD hit out of the 16 cells it controls and stores up to 16 hit data as long as the hits occur on different channels. The digital info (address, high threshold) is memorized in registers. At the same time, the analog one is recorded by the peak stretcher of each channel, gaining successive access to the output (MUX) when a DAQ Acknowledge signal (ACK) goes low. The first analog data is delivered without external input, while the digital lines, organized in buses, wait the chip ACK, to avoid bus conflicts. At the end of the event readout, an optional Master Reset (MR) is sent by the DAQ, emptying all registers and resetting the peak stretchers. All SFERA parameters (individual channel gain, shaping times, channel thresholds and LT signal width) are programmable. The 24 SFERA chips are grouped in 6 DAQ buses sharing the address lines and the FPGA-ASIC control signals, while the analog outputs, internally multiplexed by SFERA, have dedicated low-noise cabling and driver circuitry, reaching independent ADCs (NI PCI-6115), operated at 10 Ms/s with FPGA generated clocks. At least 4 conversions are performed for each data sample, to reduce the EMI interference. Each of the 6 ADC boards acquires the outputs of 4 SFERA chips handling 64 SDD channels installed on a single digital bus. Two parallel FPGA loops are continuously running; one monitors the presence of the trigger signal, while the other checks the LT signal lines. Once the last is detected, it starts the SDD DAQ procedure. If a trigger has no corresponding SDD signals, only the trigger and the veto scintillators are recorded. If the LTs weren't preceded by a trigger, only the SDD signals will be acquired. When both are present, the SDD chains record also the trigger mark and the corresponding charge packets drift time. A complex FPGA-driven sparse readout algorithm, adapted for high instantaneous rates and multiplicities (bursts) identifies the full event structure, organizes the data queues and provides the bus access, the ASIC control signals and the ADC sampling clocks. The algorithm, running on two NI PCI-7813 (currently upgraded to NI PCIe-7822) is written in LabVIEW FPGA and comprises 27 processing chains with pyramidal organization, allowing acquiring extremely high hit rates (4 Mevents/s/bus, average). This performance consents covering any accelerator condition, including the high-background-rate periods of beam injection (part of which are used in the final data analysis), with a single industrial PC crate equipped with 9 DAQ boards (6 ADCs, 2 FPGA, 1 VME). A schematic layout of the data flow and the associated connections for 1 DAQ bus is presented in figure 21.



2024 JINST 19 P11006

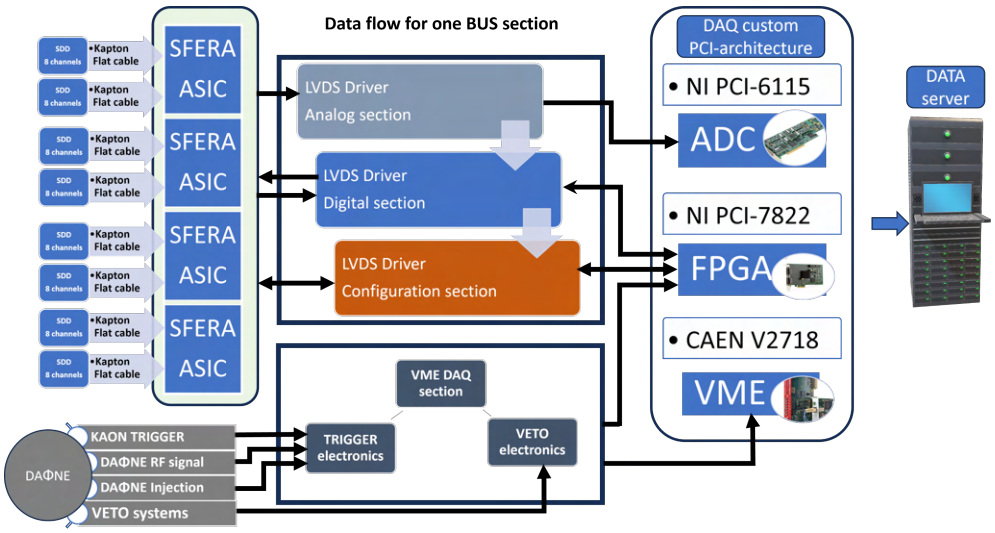


**Figure 21.** Data flow chart for one BUS of the DAQ.

## 4 Conclusions

The DAΦNE collider at INFN-LNF stands out as the optimal source of kaons for conducting highly accurate measurements on kaonic atoms. The installation of the SIDDHARTA-2 apparatus has successfully been concluded during the commissioning phase of the collider. The setup, incorporating a series of enhancements over its SIDDHARTA predecessor, has demonstrated its effectiveness and suitability for the demanding task of precision spectroscopy of kaonic atoms [25–27]. The SIDDHARTA-2 experiment is currently taking data for the measurement of kaonic deuterium, initiated in the spring of 2023 and targeting 800 $pb^{-1}$ of data. The experiment aims providing a kaonic deuterium measurement at the same level of precision as the kaonic hydrogen one, thus concluding a long-awaited determination of isospin dependent kaon-nucleon scattering lengths. Following the completion of the ongoing kaonic deuterium project, further experiments have been proposed at DAΦNE [28, 29], with important goals like the determination of the precise mass of the charged kaon, the spectroscopy of heavier kaonic atoms and the measurement of low momenta kaon-nucleon scattering amplitudes.

## Acknowledgments

We thank C. Capoccia from LNF-INFN and H. Schneider, L. Stohwasser, and D. Pristauz-Telsnigg from Stefan-Meyer-Institut for their fundamental contribution in designing and building the SIDDHARTA-2 setup. We thank as well the DAΦNE staff for the excellent working conditions and permanent support. Part of this work was supported by the Austrian Science Fund (FWF): [P24756-N20 and P33037-N]; the Croatian Science Foundation under the project IP-2022-10-3878; the MEXT Grants-in-Aid 18H05402 and 22H00122; EU STRONG-2020 project (grant agreement No. 824093); the EU Horizon 2020 project under the MSCA G.A. 754496; the EXOTICA project of the Minstero degli Affari Esteri e della Cooperazione Internazionale, PO22MO03; the Polish Ministry of Science and Higher Education grant No. 7150/E-338/M/2018; the Polish National Agency for Academic Exchange (grant No. PPN/BIT/2021/1/00037); the SciMat and qLife Priority Research Areas budget under the program Excellence Initiative – Research University at the Jagiellonian University.



2024 JINST 19 P11006

## References


[1] C. Curceanu et al., *The modern era of light kaonic atom experiments*, *Rev. Mod. Phys.* **91** (2019) 025006.

[2] M. Iwasaki et al., *Observation of the kaonic hydrogen $K_\alpha$ x-ray*, *Phys. Rev. Lett.* **78** (1997) 3067.

[3] SIDDHARTA collaboration, *A New Measurement of Kaonic Hydrogen X-rays*, *Phys. Lett. B* **704** (2011) 113 [arXiv:1105.3090].

[4] SIDDHARTA collaboration, *Preliminary study of kaonic deuterium X-rays by the SIDDHARTA experiment at DAFNE*, *Nucl. Phys. A* **907** (2013) 69 [arXiv:1302.2797].

[5] A. Gal, *On the scattering length of the $K^-d$ system*, *Int. J. Mod. Phys. A* **22** (2007) 226 [nucl-th/0607067].

[6] M. Döring and U.-G. Meißner, *Kaon–nucleon scattering lengths from kaonic deuterium experiments revisited*, *Phys. Lett. B* **704** (2011) 663 [arXiv:1108.5912].

[7] N.V. Shevchenko, *Near-threshold $K^-d$ scattering and properties of kaonic deuterium*, *Nucl. Phys. A* **890-891** (2012) 50 [arXiv:1201.3173].

[8] T. Mizutani, C. Fayard, B. Saghai and K. Tsushima, *Faddeev-chiral unitary approach to the $K^-d$ scattering length*, *Phys. Rev. C* **87** (2013) 035201 [arXiv:1211.5824].

[9] Z.-W. Liu, J.-J. Wu, D.B. Leinweber and A.W. Thomas, *Kaonic Hydrogen and Deuterium in Hamiltonian Effective Field Theory*, *Phys. Lett. B* **808** (2020) 135652 [arXiv:2003.09181].

[10] Particle Data Group, *Review of Particle Physics*, *PTEP* **2020** (2020) 083C01.

[11] M. Zobov et al., *Test of crab-waist collisions at DAΦNE Φ factory*, *Phys. Rev. Lett.* **104** (2010) 174801.

[12] M. Skurzok et al., *Characterization of the SIDDHARTA-2 luminosity monitor*, 2020 *JINST* **15** P10010 [arXiv:2008.05472].

[13] T. Koike, T. Harada and Y. Akaishi, *Cascade calculation of $K^-$-p and $K^-$-d atoms*, *Phys. Rev. C* **53** (1996) 79.

[14] E. Gatti and P. Rehak, *Semiconductor drift chamber — An application of a novel charge transport scheme*, *Nucl. Instrum. Meth. A* **225** (1984) 608.

[15] L. Bombelli et al., *Low-noise CMOS charge preamplifier for X-ray spectroscopy detectors*, in the proceedings of the *IEEE Nuclear Science Symposuim & Medical Imaging Conference*, Knoxville, TN, U.S.A., October 30–November 6 (2010) [DOI:10.1109/nssmic.2010.5873732].

[16] R. Quaglia et al., *Development of arrays of Silicon Drift Detectors and readout ASIC for the SIDDHARTA experiment*, *Nucl. Instrum. Meth. A* **824** (2016) 449.

[17] F. Schembari, R. Quaglia, G. Bellotti and C. Fiorini, *SFERA: An Integrated Circuit for the Readout of X and $\gamma$-Ray Detectors*, *IEEE Trans. Nucl. Sci.* **63** (2016) 1797.

[18] M. Miliucci et al., *Energy Response of Silicon Drift Detectors for Kaonic Atom Precision Measurements*, *Condens. Mat.* **4** (2019) 31.

[19] M. Miliucci et al., *Silicon drift detectors system for high-precision light kaonic atoms spectroscopy*, *Measur. Sci. Tech.* **32** (2021) 095501.

[20] M. Bazzi et al., *Characterization of the SIDDHARTA-2 second level trigger detector prototype based on scintillators coupled to a prism reflector light guide*, 2013 *JINST* **8** T11003.

[21] M. Tüchler et al., *A charged particle veto detector for kaonic deuterium measurements at DAΦNE*, *J. Phys. Conf. Ser.* **1138** (2018) 012012.


2024 JINST 19 P11006

[22] M. Tüchler, *Probing the strong interaction with kaonic atom X-ray measurements at low energies*, Ph.D. thesis, Vienna University, Vienna, Austria (2023).

[23] M. Tüchler et al., *The SIDDHARTA-2 Veto-2 system for X-ray spectroscopy of kaonic atoms at DAΦNE*, 2023 *JINST* **18** P11026.

[24] K. Toho, *Development and performance evaluation of particle identification detector and trace detector for kn interaction research at DAΦNE*, M.Sc. thesis, Tohoku University, Sendai Japan (2023).

[25] F. Sgaramella et al., *Measurements of high-n transitions in intermediate mass kaonic atoms by SIDDHARTA-2 at DAΦNE*, *Eur. Phys. J. A* **59** (2023) 56 [arXiv:2304.11352].

[26] D. Sirghi et al., *A new kaonic helium measurement in gas by SIDDHARTINO at the DAΦNE collider*, *J. Phys. G* **49** (2022) 055106 [arXiv:2201.09735].

[27] F. Sgaramella et al., *Kaonic atoms measurements with SIDDHARTA-2*, *J. Phys. Conf. Ser.* **2446** (2023) 012023.

[28] C. Curceanu et al., *Kaonic Atoms Measurements at DAΦNE: SIDDHARTA-2 and Future Perspectives*, *Few Body Syst.* **62** (2021) 83.

[29] C. Curceanu et al., *Fundamental physics at the strangeness frontier at DAΦNE. Outline of a proposal for future measurements*, arXiv:2104.06076.

2024 JINST 19 P11006